Electron Super-Rich Radicals. III. On the Peculiar Behavior of the Aminodihydroxymethyl Radical in the Gas Phase

Joshua A. Gregersen, Changtong Hao, and František Tureček*

Department of Chemistry, University of Washington, Bagley Hall, Box 351700, Seattle, Washington 98195-1700

Received: March 4, 2009; Revised Manuscript Received: April 16, 2009

In contrast to previously reported electron-super-rich trihydroxy-, triamino- and diaminohydroxymethyl radicals, the title aminodihydroxymethyl radical (**1**) generates a fraction of metastable species in the form of their deuterium isotopologues. The lifetimes of metastable radicals produced by femtosecond collisional electron transfer to aminodihydroxymethyl cations exceed 4 μs. The main fraction of **1** dissociates by fast loss of a hydroxyl hydrogen atom to form carbamic acid. Loss of an amino hydrogen atom is less facile and becomes <10% competitive at high internal energies or if the main dissociation is slowed down by deuterium isotope effects. RRKM calculations of unimolecular rate constants on a CCSD(T)/aug-cc-pVTZ potential energy surface gave a reasonably good fit for the competitive dissociations of **1** but not for the fraction of nondissociating radicals. The metastable species are attributed to excited electronic states which are predicted to have favorable Franck−Condon factors for being formed by collisional electron transfer.

Introduction

The carbamate group, $R_2N-COOR'$,[1] is a common component of many organic molecules, for example, as protecting *tert*-butyloxycarbamate (*t*-Boc) and 9-fluorenylmethylcarbamate (Fmoc) groups used in peptide synthesis, in drugs, for example, the cholinesterase inhibitor neostigmine, and numerous pesticides. Carbamates are also formed as intermediates in several biochemical cycles.[2] In contrast, free carbamic acid is unstable in solution, where it decomposes to ammonia and carbon dioxide, a feature which is utilized in removing peptide protecting groups.[3]

The highly rarefied gas phase existing in the vacuum system of a mass spectrometer provides an inert medium for the generation and studies of reactive ions and elusive molecules.[4] Thus, free carbamic acid has been generated in an isolated state in the gas phase,[5] ionized to a stable cation radical, and characterized by neutralization−reionization mass spectrometry (NRMS).[6] Dissociations of gas-phase carbamate ester ions have also been studied.[7] We have recently reported on the generation and properties of electron-rich carbon-centered radicals in which the carbon atom was flanked by π-donating hydroxy and amino groups.[8,9] Radicals $C(OH)_3$,[8] $C(OH)(NH_2)_2$, and $C(NH_2)_3$[9] have been generated as transient species from their cation precursors by femtosecond electron transfer, and their dissociations were studied by NRMS. Neutralization of cations followed by reionization of neutral intermediates to cations is denoted by $^+NR^+$.[10] As a rule, these electron-rich radicals dissociated rapidly on the microsecond time scale, so that no surviving species could be detected after collisional reionization. A conspicuous feature of these radicals was their extremely low ionization energies (4.29−5.88 eV),[9] which elicited comparison with those of alkali metal atoms.[11] Another general feature of electron-rich radicals was large Franck−Condon effects in vertical electron transfer, which originated from very different relaxed geometries of the precursor ions and radicals and which were associated with substantial vibrational excitation that drove radical dissociation.

Here, we report on the generation of the aminodihydroxymethyl radical (**1**), which is the remaining electron-super-rich radical containing a combination of amino and hydroxyl groups. Radical **1** is formally derived from carbamic acid by hydrogen atom addition to the carbonyl group. We wish to show that radical **1** exhibited some unusual properties when generated by femtosecond electron transfer as studied by experiment and theory.

Experimental Section

Materials. Urethane, butyl carbamate, dimethyl disulfide, trichloroacetic acid, and sodium cyanate (all Sigma-Aldrich) were used as received. D_2O and ethanol-d_5 (both Cambridge Isotope Laboratories) were used as received. (Amino-d_2)-urethane and (amino-d_2)-butyl carbamate were prepared by H/D exchange as follows. An amount of 0.5 g of urethane or butyl carbamate was dissolved in 3 mL of D_2O and stirred for 1 h. The solvent was evaporated in vacuo, and the solid was used for analysis. Butyl carbamate was heated to ∼50 °C to facilitate solvation in D_2O. (Ethyl-d_5)-carbamate was prepared according to the procedure of Modarresi[12] with the substitution of ethanol-d_5.

Methods. Neutralization−reionization mass spectra were collected on the University of Washington tandem quadrupole acceleration−deceleration mass spectrometer described previously.[13] Cations were generated in an electron impact (EI) source or by charge exchange (CE) in a chemical ionization source. Typical ionization conditions were a 500 μA emission current for EI and a 1 mA emission current for CE. The electron energy was 70 eV for the EI source and was tuned for the best signal in CE but was typically 100 eV. The source temperature was 240−280 °C for EI and 260−300 °C for CE. Samples were introduced through a room-temperature direct probe. Xenon was used for CE at a pressure of 1×10^{-5} Torr as read on an ionization gauge located at the diffusion pump intake. Precursor cations were extracted from the ion source and passed through

* To whom correspondence should be addressed.

10.1021/jp9019987 CCC: $40.75
Published on Web 04/30/2009

a quadrupole mass filter operated in the radio-frequency-only mode, accelerated to a total kinetic energy of 7170 eV, and neutralized in the collision cell floated at −7170 V. Dimethyl disulfide (DMDS) was introduced to the differentially pumped collision cell at a pressure to achieve 70% transmittance of the precursor ion beam. The ions and neutrals were allowed to drift to a four-segment conduit, where the ions were reflected by the first segment floated at +250 V. The neutral drift time through the conduit was 4.0−4.1 μs. The fast neutral species were reionized in the second collision cell with oxygen at a pressure to achieve 70% transmittance of the precursor ion beam. The ions formed in the second collision cell were decelerated, the fast neutrals were blocked by a chicane lens that also provided an ion kinetic energy filter, and the ions passing the filter were analyzed by a second quadrupole mass filter operated at unit mass resolution. The decelerating potential and the quadrupole mass filter were scanned in a linked fashion to transmit ions of a selected mass and kinetic energy. Typical spectra consisted of 30 accumulated repetitive scans, and each spectrum was reproduced at least three times over a period of many weeks. Variable-time measurements were performed as described previously.[14] The flight times of the neutral intermediates that were used to evaluate the unimolecular dissociation kinetics were 0.43, 1.18, and 1.94 μs.

High-resolution (>10,000) mass spectra and collision-induced dissociation (CID) spectra of $\mathbf{1}^+$ and its isotopologues $\mathbf{1a}^+$ and $\mathbf{1b}^+$ were measured on a JEOL HX-110 double-focusing mass spectrometer of forward geometry (the electrostatic sector E precedes the magnet B). For CID, collisions with air were monitored in the first field-free region at a pressure to achieve 70 and 50% transmittance of the ion beam at 10 keV. The spectra were obtained by scanning E and B simultaneously while maintaining a constant B/E ratio (B/E linked scan).

Calculations. Standard ab initio calculations were performed using the Gaussian 03 suite of programs.[15] Geometries for ions, neutral molecules, radicals, and transition states were optimized with Becke's hybrid functional (B3LYP)[16] and the 6-311+G(d,p) basis set. Optimization of several key species with B3LYP/6-311++G(d,p) provided structures that were within 0.001 Å, 0.3°, and 0.7° for bond lengths, bond angles, and dihedral angles, respectively, of those from B3LYP/6-311+G(d,p) optimizations. Thus, the two sets were considered identical. The optimized structures were characterized by harmonic frequency analysis as local minima (all frequencies real) or as first-order saddle points (one imaginary frequency). First-order saddle points were further characterized by intrinsic reaction coordinate analysis. Zero-point vibrational energies (ZPVE) were calculated from B3LYP/6-311+G(d,p) frequencies, which were scaled by 0.963.[17] The rigid rotor harmonic oscillator approximation was used in all thermochemical calculations. The B3LYP optimized geometries were used for single-point energy calculations using MP2 and B3LYP with the larger 6-311++G(3df, 2p) basis set and with Dunning's correlation-consistent triple-ζ basis set augmented with polarization and diffuse functions on all atoms, aug-cc-pVTZ.[18] Single-point coupled cluster[19] calculations with single, double, and disconnected triple excitations of valence electrons (CCSD(T))[20] were performed with the large aug-cc-pVTZ basis set for selected local energy minima and transition states.

Franck−Condon energies in vertical neutralization and reionization were taken as the difference between CCSD(T) energies of optimized ion and neutral structures and those in which and electron has been added to an optimized cation structure or subtracted from an optimized neutral structure. Vertical transitions between electronic states were addressed by time-dependent density functional theory (TD-DFT)[21] calculations using B3LYP and the aug-cc-pVTZ basis set. Local energy minima corresponding to excited electronic states were addressed by configuration-interaction singles (CIS) calculations[22] with the 6-311+G(d,p) basis set.

SCHEME 1

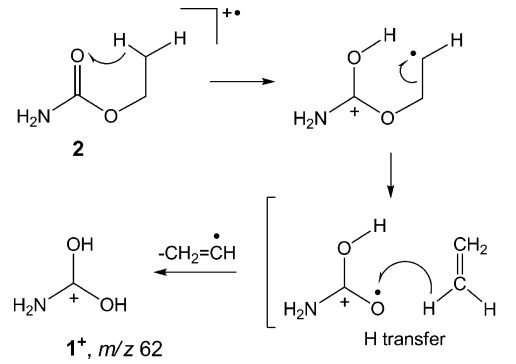

Unimolecular rate constants were calculated by Rice−Ramsperger−Kassel−Marcus (RRKM) theory[23] using Zhu and Hase's[24] program that was recompiled for Windows XP.[25] The RRKM rate constants were obtained by direct count of quantum states in 0.5 kJ mol^{-1} steps from the transition-state energy up to 250 kJ mol^{-1} above the reactant. Rotations were treated adiabatically, and the calculated $k(E,J,K)$ microscopic rate constants were Boltzmann-averaged over the thermal distribution of rotational states at 523 K, corresponding to the ion source temperature, to provide canonical rate constants $k(E)$. Tunneling effects were not considered.

Results and Discussion

Preparation of $C(NH_2)(OH)_2^+$ Cations and Isotopomers. Cation $\mathbf{1}^+$ was generated by dissociative ionization of alkylcarbamates that give the corresponding m/z 62 peak (CH_4NO_2) as a major fragment ion in the 70 eV electron ionization mass spectrum.[26] The first step of the ion dissociation is a γ-hydrogen rearrangement, which is followed by elimination of an alkenyl radical with a proton transfer, as shown for urethane in Scheme 1. Urethane (**2**) and *n*-butyl carbamate (**3**) were both used as precursors for the production of $\mathbf{1}^+$.

High-resolution mass spectra confirmed the absence of any isobaric interference at m/z 62. The deuterium-labeled ion $C(ND_2)(OH)_2^+$ ($\mathbf{1a}^+$, m/z 64) was produced from (amino-d_2)-urethane (**4**) and (amino-d_2)-butyl carbamate (**5**). The complementary labeled ion $C(NH_2)(OD_2)^+$ ($\mathbf{1b}^+$, m/z 64) was produced from (ethyl-d_5)-urethane (**6**) as shown in Scheme 2.

Ion Dissociations. High-resolution mass spectra confirmed the elemental composition of the fragment at m/z 62 (62.0242) as CH_4NO_2. Collision-induced dissociation (CID) mass spectra of $\mathbf{1}^+$ showed the formation of $CONH_2^+$ (m/z 44) and $COOH^+$ (m/z 45) by elimination of water and ammonia, respectively, as the major dissociation channels. (Figure S1a−d, Supporting Information). Formation of $CONH_2^+$ was preferred over $COOH^+$ by a 2:1 ratio. Other, less abundant fragments corresponded to loss of H (m/z 61) and formation of COH^+ (m/z 29) and NH_x ($x = 2-4$) fragments at m/z 16−18.

The CID spectrum of $\mathbf{1}^+$ that was generated from two different precursors (**2** and **3**) were very similar with the exception of the m/z 61 fragment, which was more abundant in the CAD spectrum of $\mathbf{1}^+$ from **2** (Figure S1a,b) Deuterium labeling ($\mathbf{1a}^+$) confirmed the peak assignment based on mass

SCHEME 2

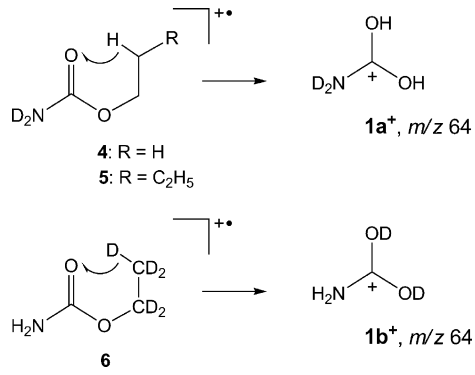

shifts of *m/z* 44 → *m/z* 46 ($COND_2^+$), *m/z* 44 → *m/z* 45 ($COOD^+$), *m/z* 18 → *m/z* 20 ($NH_2D_2^+$), and *m/z* 17 → *m/z* 19 ($NHD_2^{+\bullet}$). Likewise, the CAD spectrum of **1b**$^+$ showed mass shifts of *m/z* 45 → *m/z* 46 ($COOD^+$), *m/z* 29 → *m/z* 30 (COD^+), *m/z* 18 → *m/z* 20 ($NH_2D_2^+$), and *m/z* 17 → *m/z* 18 ($NH_2D^{+\bullet}$). The *m/z* 44 peak showed only a partial mass shift to *m/z* 45, which indicated some H/D exchange in the elimination of water. The loss of H/D from **1a**$^+$ and **1b**$^+$ (*m/z* 63 and 62, respectively) showed no selectivity depending on the deuterium position in the precursor ion.

Ion Structures and Energies. To further characterize the ions, we obtained the optimized structures for **1**$^+$, its isomers, and interconnecting transition states (Figure 1). The ion relative and dissociation energies are summarized in Table 1 and visualized in a potential energy diagram (Figure 2). The energies presented in the text and Figure 2 are from CCSD(T)/aug-cc-pVTZ single-point calculations and refer to 0 K. Three conformers (anti−syn-**1**$^+$, anti−anti-**1**$^+$, and syn−syn-**1**$^+$) were found as local energy minima for **1**$^+$, with anti−syn-**1**$^+$ being the lowest-energy rotamer, presumably owing to a favorable orientation of the O−H and N−H bond dipoles. Relative to anti−syn-**1**$^+$, anti−anti-**1**$^+$ and syn−syn-**1**$^+$ were 5 and 21 kJ mol^{-1} higher in energy, respectively, and were separated from it by rotational energy barriers of 24 and 43 kJ mol^{-1}, respectively (**TS1** and **TS2**, Figure 2). Since the conformers of **1**$^+$ are derived by protonation of carbamic acid (**9**), their relative energies with respect to **9** provide the proton affinity and gas-phase basicity of the latter at 298 K as PA = 822 and GB = 787 kJ mol^{-1} for anti−syn-**1**$^+$. The CCSD(T)/aug-cc-pVTZ value for PA(**9**) agrees reasonably well with the G2MP2-calculated value reported recently[27] but is higher than the MP2 values reported earlier.[28]

A fourth isomer (**7**$^+$) was identified as a local energy minimum that was an adduct of ammonia to $COOH^+$. Ion **7**$^+$ was 41 kJ mol less stable than anti−syn-**1**$^+$, and the two were separated by a substantial energy barrier of 193 kJ mol^{-1} in **TS3**. Dissociation of anti−syn-**1**$^+$ to NH_3 + $COOH^+$ required 261 kJ mol^{-1} and most likely involved **7**$^+$ as an intermediate. Dissociation of anti−syn-**1**$^+$ to H_2O + $CONH_2^+$ required 158 kJ mol^{-1} at the thermochemical threshold and an energy barrier of 206 kJ mol^{-1} in **TS4**.

A fifth isomer of **1**$^+$ was an ion−molecule complex of NH_4^+ and CO_2 (**8**$^+$), which was the global energy minimum of the present set of ions. Ion **8**$^+$ was 84 kJ mol^{-1} more stable than anti−syn-**1**$^+$. The energy barrier for anti−syn-**1**$^+$ → **8**$^+$ is unknown but requires at least two hydrogen migrations possibly involving **7**$^+$ as an intermediate. Attempts to experimentally generate and characterize the $NH_4^+\cdots CO_2$ complex were unsuccessful. However, dissociations of **8**$^+$ can be reasonably expected to form NH_4^+ rather than $COOH^+$ because of the much larger proton affinity of ammonia (854 kJ mol^{-1}) compared to that of CO_2 (541 kJ mol^{-1}).[26] Note that the dissociation of **8**$^+$ to NH_4^+ and CO_2 is only 54 kJ mol^{-1} endothermic. If **8**$^+$ was formed by isomerization of **1**$^+$ through **TS3**, it would acquire ∼280 kJ mol^{-1} of internal energy from passing over the isomerization barrier and would be likely to rapidly dissociate. Furthermore, we would expect a much larger relative abundance in the CAD mass spectrum of NH_4^+ (*m/z* 18) and a much smaller relative abundance of $COOH^+$ (*m/z* 45) if the ion−molecule complex **8**$^+$ was a significant contributor. In summary, the CAD spectra strongly indicate that the *m/z* 62 ion from **2** and **3** has the bond connectivity of **1**$^+$ and presumably consists of its anti−syn and anti−anti conformers.

Radical Formation and Dissociations. Neutralization of **1**$^+$ followed by reionization showed no survivor ion at *m/z* 62 in the $^+NR^+$ mass spectrum that would have indicated a fraction of radical **1** with >4 μs lifetimes (Figure 3a). The major

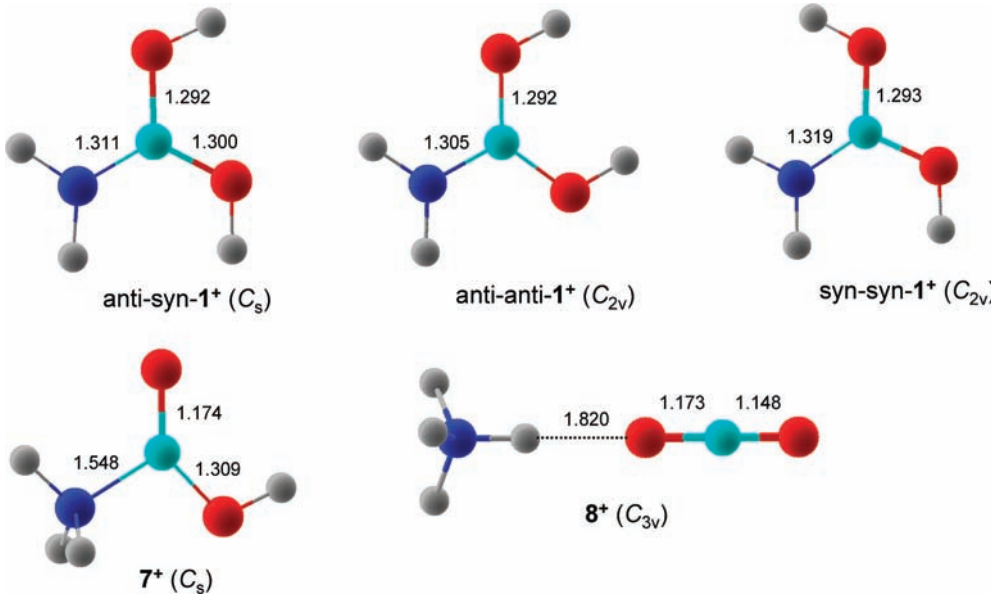

Figure 1. B3LYP/6-311+G(d,p) optimized structures of $[CH_4O_2N]^+$ cations. Bond lengths in Ångstroms. The atoms are color coded as follows: red, O; blue, N; turquoise, C; gray, H.

TABLE 1: Ion Relative Energies and Proton Affinities

	Relative Energy[a,b]				
	B3LYP			MP2	CCSD(T)
ion/reaction	6-311+G(d,p)	6-311++G(3df,2p)	aug-cc-pVTZ	6-311++G(3df,2p)	aug-cc-pVTZ
anti−syn-$\mathbf{1}^+$	0	0	0	0	0
anti−anti-$\mathbf{1}^+$	6	5	4	5	5
syn−syn-$\mathbf{1}^+$	25	21	21	21	21
$\mathbf{7}^+$	41	48	50	36	41
$\mathbf{8}^+$	−97	−86	−83	−103	−84
TS1 (anti−syn-$\mathbf{1}^+$ → anti−anti-$\mathbf{1}^+$)	24	24	24	26	24
TS2 (anti−syn-$\mathbf{1}^+$ → syn−syn-$\mathbf{1}^+$)	44	42	42	44	43
TS3 (anti−syn-$\mathbf{1}^+$ → $\mathbf{7}^+$)	195	199	198	191	193
NH_3 + $COOH^+$	260	260	261	249	261
H_2O + $CONH_2^+$	150	156	156	147	158
TS4 (anti−syn-$\mathbf{1}^+$ → H_2O + $CONH_2^+$)	205	207	205	202	206
$\mathbf{1}^+ \rightarrow \mathbf{9}^{+\bullet}$ + H•	485	489	490	539	511
PA at C=O[c]	814	822	824	808	822
GB at C=O[d]	780	788	790	774	787
PA at NH_2[c]	772	773	774	771	780
GB at NH_2[d]	742	743	743	741	750

[a] In units of kJ mol^{-1}. [b] Including B3LYP/6-311+G(d,p) zero-point energies and referring to 0 K. [c] Topical proton affinities in carbamic acid at 298 K. [d] Topical gas-phase basicities in carbamic acid at 298 K.

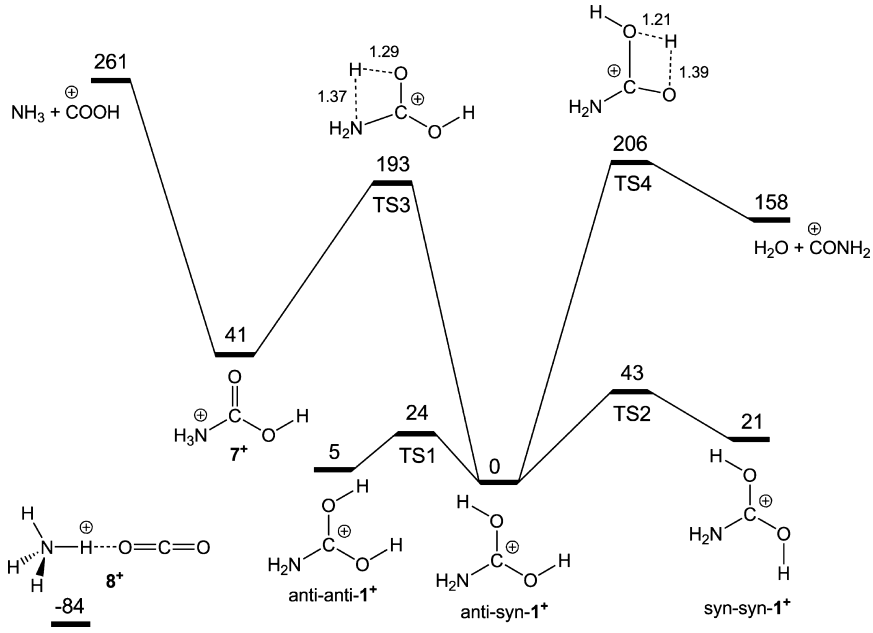

Figure 2. Potential energy diagram for isomerizations and dissociations of $[CH_4O_2N]^+$ cations. Energies from CCSD(T)/aug-cc-pVTZ calculations include B3LYP/6-311+G(d,p) zero-point corrections.

fragments in the $^+NR^+$ mass spectrum were $[C,H_3,N,O_2]$ (loss of H), COOH, CO_2 or $CONH_2$, CONH, NCO, COH, CO, NH_3, OH, and NH_2 at *m/z* 61, 45, 44, 43, 42, 29, 28, 17, 17, and 16, respectively. The $^+NR^+$ mass spectrum of $\mathbf{1}^+$ prepared from **3** also showed no survivor ion (Figure S2, Supporting Information). The two $^+NR^+$ mass spectra displayed minor differences in the fragment relative intensities, for example, for *m/z* 29 and 16. Note that the peak at *m/z* 32 in the $^+NR^+$ mass spectra originates from collisional ionization of O_2 diffusing from the reionization cell. The fragments observed in the $^+NR^+$ mass spectra of $\mathbf{1}^+$ are practically the same as those obtained by NRMS of carbamic acid (**9**),[5] indicating that the latter can be an intermediate of dissociations of **1**.

Deuterium labeling ($\mathbf{1a}^+$ and $\mathbf{1b}^+$) caused major effects in the $^+NR^+$ mass spectra (Figure 3b,c). In contrast to $\mathbf{1}^+$, both $\mathbf{1a}^+$ and $\mathbf{1b}^+$ prepared by dissociative ionization at 70 eV reproducibly gave a fraction of survivor ions at *m/z* 64, indicating that radicals **1a** and **1b** of ∼4 μs lifetimes were produced. The intensities of survivor $\mathbf{1a}^+$ and $\mathbf{1b}^+$ ions were 1.5 and 1.8% relative to the sum of NR ion intensities. However, when ions $\mathbf{1}^+$, $\mathbf{1a}^+$, and $\mathbf{1b}^+$ were produced by dissociative charge exchange ionization with Xe, their $^+NR^+$ mass spectra displayed no survivor ions, while the fragment relative intensities were virtually the same as those for ions prepared by 70 eV electron ionization. Charge exchange ionization with Xe (IE =12.13 and 13.44 eV for the $^2P_{3/2}$ and $^2P_{1/2}$ bands) was expected to produce $\mathbf{1}^+$ of a lower internal energy, which was further moderated by collisions with thermal Xe atoms in the high-pressure ion source. We note that at the typical ion source temperatures of 200−250 °C, ion $\mathbf{1}^+$ is calculated to have a rovibrational enthalpy of 20−24 kJ mol^{-1}.

Loss of light or heavy hydrogen atoms showed 97% selectivity for the loss of H from **1a** and 90% selectivity for the loss of D from **1b**. This was established by multiscan measurements of NR ion intensities in the narrow *m/z* 60−65 region to improve the signal-to-noise ratios for these low-intensity ions (Figure

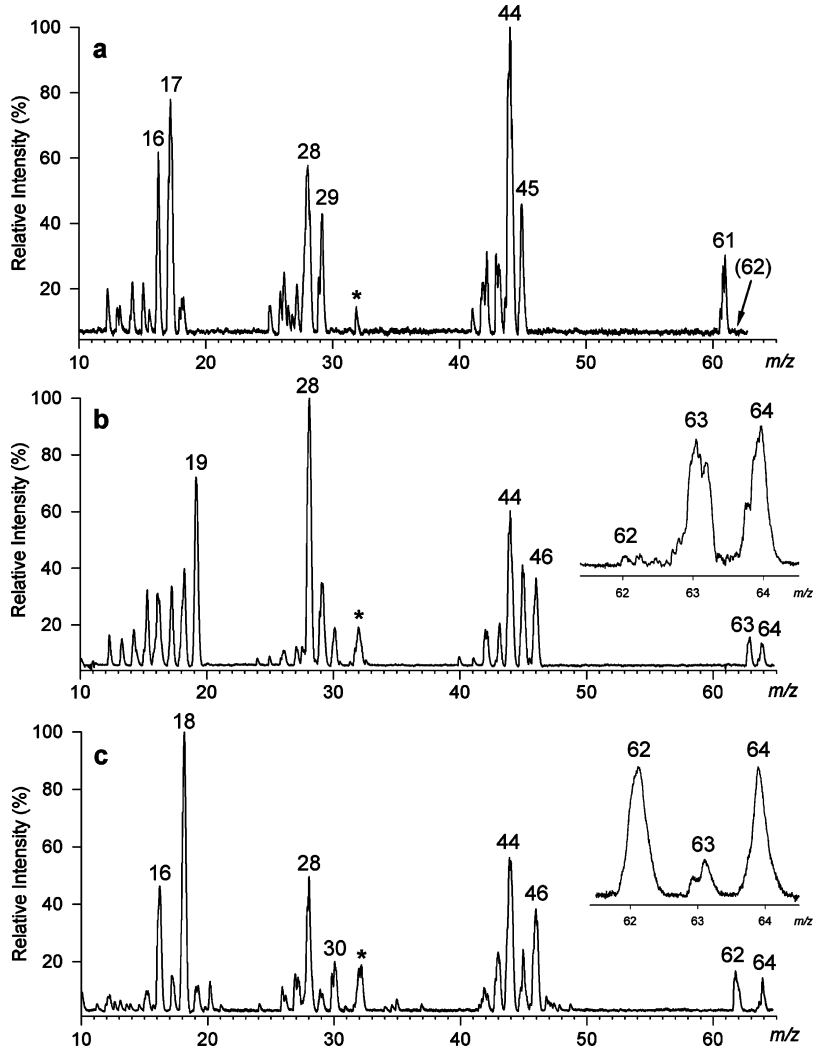

Figure 3. $^{+}NR^{+}$ mass spectra (CH_3SSCH_3, 70% transmittance/O_2, 70% transmittance) of (a) $\mathbf{1}^+$, (b) $\mathbf{1a}^+$, and (c) $\mathbf{1b}^+$. Insets show the *m*/*z* 61−65 regions from separate 200 scan measurements.

3b,c insets). The high selectivity for the O−(H,D) bond cleavage in **1a** and **1b** was very different from the loss of H/D in CAD of the respective ions where no selectivity was observed (Figure S1c,d, Supporting Information). Thus, the $^{+}NR^{+}$ mass spectra indicated that the loss of H atoms mainly occurred in the radical intermediates, not by ion dissociations after reionization.

The other NR dissociations also showed characteristic mass shifts caused by deuterium labeling. For example, the *m*/*z* 45 peak (loss of NH_3 from **1**) partially shifted to *m*/*z* 46 in both **1a** and **1b**. The *m*/*z* 44 peak showed partial retention at the same mass in **1a** and **1b** and partial shift to *m*/*z* 45 and 46. This indicated that the *m*/*z* 44 fragment was a mixture of CO_2 and $CONH_2$ and that the eliminations of water and ammonia were accompanied by partial H/D exchange between the amino and hydroxyl groups. Likewise, the *m*/*z* 28 fragment was mostly CO because of its mass retention when formed from **1a** and **1b**. The *m*/*z* 17 peak was mostly ammonia judged by the shift to *m*/*z* 19 in the NR spectrum of **1a**.

Radical Dissociation Kinetics. Standard NR mass spectra display fragments from dissociations of neutral intermediates which are superimposed on those occurring in ions after collisional reionization. Another possible source of NRMS fragments is collisional activation of the precursor ion causing its dissociations and detection of neutral fragments after reionization. Obviously, these three types of dissociations involve different reactants and occur on different potential energy surfaces.[4a] To distinguish these processes, we carried out variable-time NRMS experiments[14] in which the time scales for neutral and postreionization dissociations were systematically varied and selected time-dependent ion intensities were deconvoluted for those originating from neutral and ion precursors. The time-dependent relative intensities were studied for loss of H from **1a**, which showed high selectivity and where the $CO(OH)(ND_2)^{+\bullet}$ fragment represented a primary product. The time-dependent relative intensities of *m*/*z* 64 and 63 peaks were fitted into kinetic equations to yield unimolecular rate parameters for neutral (k_N) and ion (k_i) dissociations.[14b] Least-squares fits were obtained for bimodal exponential decay in the neutral channel, including one fast ($k_N > 10^7$ s^{-1}) and one slow ($k_N = 10^4-10^6$ s^{-1}) dissociation and a single-exponential decay (k_i) in the ion channel. Solving the equations required an estimate of the reionization cross section of $CO(OH)(NH_2)$ relative to **1a**. We did this according to the Fitch−Sauter scheme of atomic increments,[29] assuming that collisional reionization followed rules similar to those governing electron impact.[30] From the atomic increments for C, H, O, and N, we calculated $\sigma(CO(OH)(NH_2))/\sigma(\mathbf{1}) = 0.907$.

Elimination of hydrogen from **1a** showed contributions from both neutral dissociations and ion dissociations following reionization. For **1a** generated from urethane and butyl carbamate, the k_i values were $(0.49 \pm 0.05) \times 10^5$ and $(0.51 \pm 0.05) \times 10^5$ s^{-1}, respectively. The rate parameters for neutral

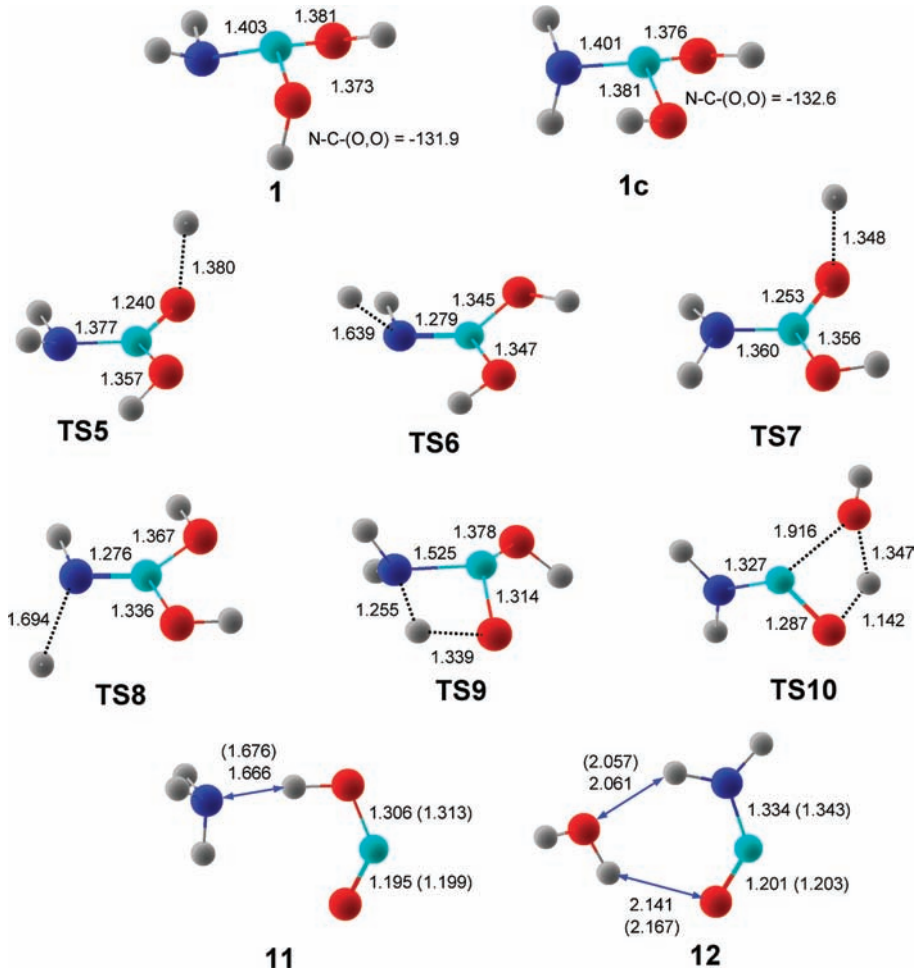

Figure 4. B3LYP/6-311+G(d,p) optimized structures of CH_4O_2N radicals. Bond lengths and atom color coding as in Figure 1.

dissociation were smaller and showed k_N values of $(0.10 \pm 0.04) \times 10^5$ and $(0.14 \pm 0.05) \times 10^5$ s^{-1} for **1a** generated from urethane and butyl carbamate, respectively. The excellent match of these results provides strong evidence for the similarity of radical **1a** as generated from urethane and butyl carbamate.

Radical Structures and Energies. To further characterize the radical intermediates produced by collisional electron transfer, we studied local energy minima and transition states for structures derived from **1**. Two stable structures were found (**1** and **1c**) that had twisted anti−syn-**1** conformations (Figure 4), whereas syn−syn-**1** and anti−anti-**1** conformers were unstable. Both stable anti−syn-**1** conformations (Figure 4) are pyramidized at C and N and show favorable orientations of the O−H and N−H bond dipoles with respect to lone electron pairs on N and O. Multiple rotations and/or umbrella inversions are necessary for interconversion of the conformers of **1**, which are presumably similar to those reported for guanidine radicals.[9] The bond rotations and umbrella inversions are expected to involve energy barriers well below the barriers to dissociation. Because conformers **1** and **1c** are nearly isoenergetic and will rapidly interchange at the experimental energy levels, we present all energies and dissociations relative to the most stable **1**.

A conspicuous feature of radical structures **1** and **1c** is that they are very different from the most stable ion structure anti−syn-$\mathbf{1}^+$. In particular, the radicals are pyramidized at the central carbon atom, whereas the ion is planar. Furthermore, the radicals show substantially longer C−O and C−N bonds (1.373−1.381 and 1.403 Å, respectively) compared to those in ion $\mathbf{1}^+$ (1.292−1.300 Å and 1.311 Å for C−O and C−N bonds, respectively). The pyramidization of C and N in **1** along with the differences in the bond lengths causes substantial Franck−Condon effects upon vertical electron transfer, which results in ∼165 kJ mol^{-1} vibrational excitation in vertically formed **1**.

Radical Dissociation Energetics. The dissociation and TS energies of **1** are summarized in Table 2 and displayed in a potential energy diagram (Figure 5). The structures of transition states and intermediates are shown in Figure 5. The dissociations that we considered included O−H and N−H bond dissociations (**TS5**−**TS8**). Because of the presence of two hydrogens on the amino group and two distinct hydrogens on the hydroxyl groups, four distinct losses of hydrogen atoms are possible. Loss of hydrogen from the hydroxyl groups to form the carbamic acid molecules anti-**9** and syn-**9** required 10 and 38 kJ mol^{-1} at the thermochemical threshold and energy barriers of 75 and 97 kJ mol^{-1} in **TS7** and **TS5**, respectively. Loss of hydrogen from the amino group to form the hydroxycarbimidic acid molecules anti−anti-**10** and anti−syn-**10** required 86 and 106 kJ mol^{-1} at the thermochemical threshold and energy barriers of 112 and 130 kJ mol^{-1} in **TS6** and **TS8**, respectively. Two additional conformations are possible as a result of dissociation of the N−H bond (syn−anti-**10** and syn−syn-**10**), but these would require bond rotation following dissociation from **1** and were thus neglected from further discussion. For both O−H and N−H bond dissociations, the lower-energy transition states (**TS7** and **TS6**) corresponded to the lower-energy conformers anti-**9** and anti−anti-**10**, respectively.

The other types of dissociations that we considered were hydrogen migrations combined with C−N and C−O bond

TABLE 2: Radical Relative Energies and Proton Affinities

	Relative Energy[a,b]				
			B3LYP	PMP2	CCSD(T)
radical/reaction	6-311+G(d,p)	6-311++G(3df,2p)	aug-cc-pVTZ	6-311++G(3df,2p)	aug-cc-pVTZ
1	0	0	0	0	0
1c	2	3	3	3	3
1 → anti-**9** + H•	10	9	11	−18	10
1 → syn-**9** + H•	43	38	41	12	38
1 → anti−anti-**10** + H•	95	92	93	65	86
1 → anti−syn-**10** + H•	118	112	113	85	106
1 → COOH• + NH_3	−9	−12	−12	−6	0
1 → $CONH_2$• + H_2O	−48	−47	−48	−41	−30
1 → **11**	−60	−57	−57	−54	−47
COOH• + NH_3 → OH• + CO + NH_3	98	101	100	111	91
COOH• +NH_3 → H• + CO_2 + NH_3	−10	−12	−9	−43	−3
$CONH_2$• H_2O → NH_2• + CO + H_2O	55	54	53	55	42
$CONH_2$• +H_2O → H• + CONH + H_2O	71	67	68	44	78
1 → **12**	−70	−66	−65	−65	−56
1 → **TS5**	83	79	80	84	97
1 → **TS6**	107	103	104	100	112
1 → **TS7**	57	55	55	59	75
1 → **TS8**	129	123	123	117	130
1 → **TS9**	140	141	140	139	142
1 → **TS10**	132	134	132	149	151
1 → **TS11**	104	111	109	113	86
1 → **TS12**	114	114	113	118	94
1 → **TS13**	84	84	85	85	106
1 → **TS14**	139	136	137	127	146

[a] In units of kJ mol^{-1}. [b] Including B3LYP/6-311+G(d,p) zero-point energies and referring to 0 K.

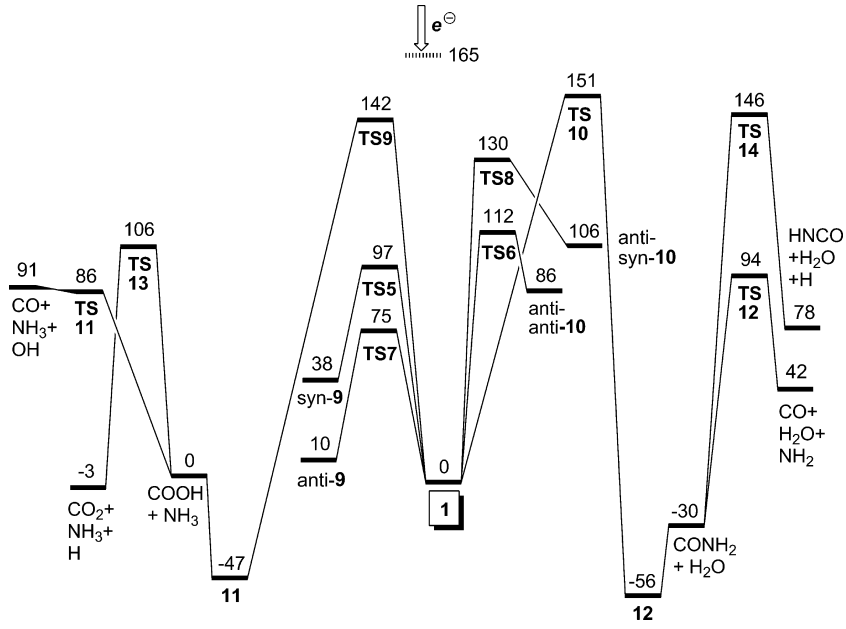

Figure 5. Potential energy diagram for isomerizations and dissociations of $[CH_4O_2N]$ radicals. Energies from CCSD(T)/aug-cc-pVTZ calculations include B3LYP/6-311+G(d,p) zero-point corrections.

cleavages and eliminations of ammonia or water (**TS9** and **TS10**, respectively). Elimination of ammonia from **1** to produce a COOH• radical requires overcoming a 142 kJ mol^{-1} energy barrier in **TS9**. **TS9** was connected to the dipole−dipole complex of ammonia with the COOH radical (**11**), which was 47 kJ mol^{-1} more stable than **1**. The overall dissociation of **1** to ammonia and COOH was virtually thermoneutral (Table 2). It is interesting to note that B3LYP calculations located another local energy minimum for an $H_3N\cdots$COOH complex which was 3 kJ mol^{-1} below **1**. However, upon reoptimization with MP2(full)/6-311+g(d,p), the latter complex collapsed to **11**. The close match between the B3LYP and MP2 optimized structures of **11** gives confidence that the structure of the complex is represented correctly.

Further dissociation of COOH• to CO and OH• requires 91 kJ mol^{-1} at the thermochemical threshold, which is below the **TS9** energy. The more energetically favorable products CO_2 and H• (−3 kJ mol^{-1} relative to **1**) are possible from consecutive dissociation of COOH• but must cross a substantial energy barrier at **TS13** of 106 kJ mol^{-1}.[31] The barrier for **TS9** indicates that COOH radicals formed from **1** would be metastable with respect to loss of OH and can be expected to have a short lifetime.

Loss of water proceeds through a single transition state **TS10** that shows an elongated C−O bond of 1.916 Å and an elongated O−H bond length of 1.142 Å. **TS10** is connected to a dipole−dipole complex of water and the $CONH_2$ radical (**12**), which is 56 kJ mol^{-1} more stable than **1**. Overall, loss of water from **1** is 30 kJ mol^{-1} exothermic, making **1** metastable with respect to this dissociation. It should be noted that elimination of water through **TS10** has the highest energy barrier (151 kJ mol^{-1}) of our calculated dissociations and would be kinetically less favorable than loss of H. Furthermore, if the energy barrier of **TS10** were crossed, the $CONH_2^{\bullet}$ product would have enough energy to undergo further dissociation to CO and $NH_2^{\bullet}$ through **TS12**.

1,2-Hydrogen migrations from OH to the carbon atom followed by dissociation of the C−H bond were also investigated but were found to be energetically disfavored by transition-state energies for hydrogen migration of 138−186 kJ mol^{-1}.

It is important to note that all transition states in Figure 5 fall below the calculated vibrational energy acquired by **1** due to Franck−Condon effects (∼165 kJ mol^{-1}) and therefore can all be considered possible dissociation pathways. Also interesting is the clustering of transition states in the 140−150 kJ mol^{-1} range, making experimental predictions based on calculations somewhat difficult because of the combination of kinetic and energetic factors controlling dissociations.

RRKM Dissociation Kinetics. The CCSD(T)/aug-cc-pVTZ potential energy surface was further used for RRKM calculations of unimolecular rate constants for the lowest-energy dissociation, which was the loss of hydrogen from **1**. Loss of $H^{\bullet}$ by O−H bond cleavages ($k_{7,O-H}$ and $k_{5,O-H}$) had lower onset energies and were faster than the competing loss of $H^{\bullet}$ by N−H bond cleavage (k_{N-H}) over the entire relevant energy range (Figure 6a). Inset in Figure 6a shows that the $k_{N-H}/(k_{7,O-H} + k_{5,O-H})$ ratio was <0.01 at internal energies <165 kJ mol^{-1} and gradually increased toward higher internal energies of **1**.

Losses of hydrogen and deuterium atoms proceeding through the low-energy dissociation channels of **1a** and **1b** were also examined. Loss of H from **1a** by O−H bond cleavages, (k(**1a**)$_{5,O-H}$) and (k(**1a**)$_{7,O-H}$) showed moderate isotope effects, for example, $k_{O-H}/k(\mathbf{1a})_{O-H} = 1.3-1.5$ at an internal energy of 165 kJ mol^{-1}. The rate constants for the competing losses of H and D from **1a** (k(**1a**)$_{5,O-H}$, k(**1a**)$_{7,O-H}$, and k(**1a**)$_{N-D}$, respectively) and **1b** (k(**1b**)$_{N-H}$, k(**1b**)$_{5,O-D}$, and k(**1b**)$_{7,O-D}$, respectively) are plotted in Figure 6b. The data indicate that the loss of the hydroxyl H or D outcompetes the loss of the amino H or D, isotope effects notwithstanding. Overall, the RRKM calculations indicated that radicals **1** formed with vibrational excitation determined by Franck−Condon effects would dissociate with rate constants of $>10^9$ s^{-1} regardless of deuterium isotope effects. While this fast dissociation is consistent with the absence of survivor radicals for **1** on the 4 μs time scale of our experiments, it contradicts the detection of surviving radicals for **1a** and **1b**. Note that detection of 0.1−1% of surviving radicals implies decay rate constants of $1.15-1.73 \times 10^6$ s^{-1}, which are 3 orders of magnitude smaller than those predicted for the dissociations of vertically formed **1**.

The energy-dependent rate constants for loss of H and D were further used to estimate the intra- and intermolecular isotope effects, which in turn were used to assess the internal energy distribution in **1a** and **1b**.[32] Estimates that were based on intramolecular isotope effects used eqs 1 and 2[32]

$$\frac{I_{\mathbf{1a},N-D}}{I_{\mathbf{1a},O-H}} = \frac{\int_{E_{TS}}^{\infty} f_{ND}(E)P(E)dE}{\int_{E_{TS}}^{\infty} f_{OH}(E)P(E)dE} \quad (1)$$

$$\frac{I_{\mathbf{1b},O-H}}{I_{\mathbf{1b},N-H}} = \frac{\int_{E_{TS}}^{\infty} f_{OD}(E)P(E)dE}{\int_{E_{TS}}^{\infty} f_{NH}(E)P(E)dE} \quad (2)$$

where $I_{\mathbf{1a},N-D}$ and so forth are the relative intensities of the respective fragments, E_{TS} is the pertinent transition-state energy, $f_{ND} = k(\mathbf{1a})_{N-D}/\{k(\mathbf{1a})_{N-D} + k(\mathbf{1a})_{5,O-H} + k(\mathbf{1a})_{7,O-H}\}$ and likewise for the other labeled compounds are the respective relative rate constants for the dissociations, and $P(E)$ is the internal energy distribution function. These simplified time-independent formulas followed from the fact that the rate constants were large, so that $\{k(\mathbf{1a})_{N-D} + k(\mathbf{1a})_{5,O-H} + k(\mathbf{1a})_{7,O-H}\}t \gg 1$ for the experimental dissociation time scale of $t = 4.1$ μs. As an internal distribution function $P(E)$, we used the normalized two-parameter formula (eq 3) reported previously[33]

$$P(E) = \frac{4(E - E_0)}{W^2} e^{-2(E-E_0)/W} \quad (3)$$

where the onset (E_0) and width (W) parameters were obtained by a least-squares fit between the experimental and RRKM-

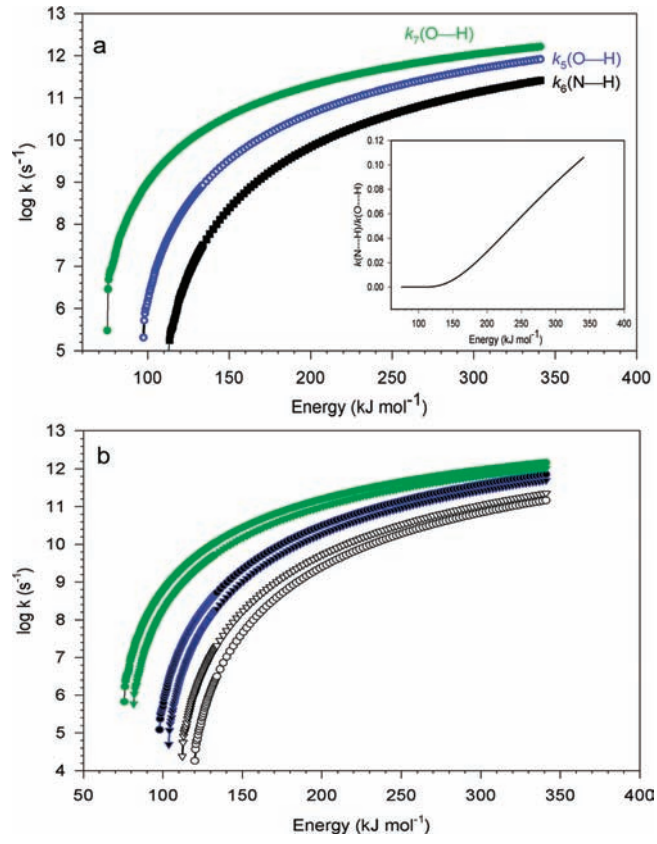

Figure 6. (a) RRKM rate constants (log k, s^{-1}) for loss of hydrogen from **1**. Open blue circles: Loss of OH hydrogen through **TS5**. Full green circles: Loss of OH hydrogen through **TS7**. Black squares: Loss of NH hydrogen through **TS6**. The inset shows the k_{N-H}/k_{O-H} branching ratio. (b) RRKM rate constants (log k, s^{-1}) for loss of hydrogen and deuterium from **1a** and **1b**. Full green circles: O−H bond dissociation through **TS7** in **1a**. Full blue circles: O−H bond dissociation through **TS5** in **1a**. Full green triangles: O−D bond dissociation through **TS7** in **1b**. Full blue triangles: O−D bond dissociation through **TS5** in **1b**. Open triangles, N−H bond dissociation through **TS6** in **1b**. Open circles, N−D bond dissociation through **TS6** in **1a**.

calculated fragment ion intensities. Using $E_0 = 155$ kJ mol^{-1} and $W = 102$ kJ mol^{-1}, we calculated $I(\mathbf{1a})_{N-D}/I(\mathbf{1a})_{O-H} = 0.040$, to be compared with the experimental value of 0.031, and $I(\mathbf{1b})_{N-H}/I(\mathbf{1b})_{O-D} = 0.07$ (experimental: 0.11). Equation 3 gives the population maximum for the internal energy of $E_{max} = E_0 + W/2 = 155 + 51 = 206$ kJ mol^{-1}. This estimate is higher than the calculated vibrational excitation due to combined Franck−Condon effects (165 kJ mol^{-1}) and the precursor ion thermal energy at the ion source temperature of 523 K (24 kJ mol^{-1}). This in turn may indicate that a fraction of precursor ions $\mathbf{1}^+$ are hyperthermal when formed by electron-impact-induced dissociation in the ion source.

The internal energy distribution and RRKM rate constants further indicated that most radicals had internal energies exceeding the energy thresholds for the most favorable dissociations by O−H and O−D bond cleavages. The relative intensities of the survivor radicals, $[\mathbf{1a}]_{rel}$ and $[\mathbf{1b}]_{rel}$, can be expressed by eqs 4 and 5, respectively

$$[\mathbf{1a}]_{rel} = \int_{E_{TS}}^{E} P(E) e^{-\{k_{5,O-H}(E)+k_{7,O-H}(E)+k_{N-D(E)}\}t} dE \quad (4)$$

$$[\mathbf{1b}]_{rel} = \int_{E_{TS}}^{E} P(E) e^{-\{k_{5,O-D}(E)+k_{7,O-D}(E)+k_{N-H(E)}\}t} dE \quad (5)$$

However, using the best-fit $P(E)$ from eqs 1 and 2 gave negligible ($<10^{-6}$ %) fractions of nondissociating **1a** and **1b** to be reionized and detected as the corresponding survivor ions. Thus, the experimentally determined fraction of surviving ions (1.5−1.8%, vide supra) was incompatible with the isotope effects upon loss of H or D if both referred to dissociations taking place on the same potential energy surface of the ground doublet electronic state shown in Figure 5.

Discussion

The RRKM kinetic modeling on the CCSD(T)/aug-cc-pVTZ potential energy surface of the ground doublet electronic state of radicals **1**, **1a**, and **1b** gave a reasonably good fit with the experimental branching ratios for loss of hydrogen and deuterium atoms from **1a** and **1b**. However, there was a discrepancy between the branching ratios and the relative intensities of nondissociating radicals, which were calculated to be much lower than the experimental data. Another peculiar feature was the rate parameters obtained from the variable-time measurements, which preferred ion dissociations against radical dissociations. According to the calculated potential energy profiles, loss of H or D from radicals **1a** and **1b** should be more favorable than the loss of H/D from reionized $\mathbf{1a}^+$ and $\mathbf{1b}^+$ as the former dissociations required transition-state energies of 75−120 kJ mol^{-1} (taking into account primary and secondary isotope effects), whereas loss of H from $\mathbf{1}^+$ was 511 kJ mol^{-1} endothermic (Table 2). Also, the magnitude of the rate parameters for the radical dissociations by loss of H (0.10−0.14 $\times 10^5$ s^{-1}) was incompatible with the RRKM rate constants, which approached 10^9 s^{-1} for radicals with the highest population probability.

One conspicuous feature of electron transfer to $\mathbf{1}^+$ is the substantial mismatch between the molecular geometries corresponding to the ion and radical potential energy minima. This has a large effect on the vibrational excitation in **1** formed in its ground electronic state, as discussed above. However, the mismatch must also have an adverse effect on the transition probability from the potential energy surface of $\mathbf{1}^+$ to that of the ground state **1** by collisional electron transfer. We used CIS calculations to investigate the first excited (^{2}A) electronic state of **1**. Upon optimization, the ^{2}A state showed a practically planar (C,N,O) frame and C−O and C−N bond lengths of 1.284−1.286 Å, which were similar to those in $\mathbf{1}^+$ (1.278−1.296 Å at the same level of theory). Because of this good geometry match, electron transfer to $\mathbf{1}^+$ is expected to have more favorable Franck−Condon factors when forming the ^{2}A electronic state than when forming the vibrationally excited ground state. Although CIS optimizations of higher electronic states of **1** did not reach convergence to give fully optimized structures, the trends for partially optimized structures again showed planar (C,N,O) frames and bond lengths close to that of the ^{2}A state. These results indicated that higher electronic excited states of **1** may also be favorably accessed by vertical electron transfer. We note that electron transfer from dimethyldisulfide to $\mathbf{1}^+$ is substantially endoergic for all electronic states of the incipient radical **1**, as judged from the relevant vertical ionization and recombination energies, for example, $IE_v(CH_3SSCH_3) = 8.96$ eV[26] and $RE_v(\mathbf{1}^+) = 3.51$ eV. The energy deficit in electron transfer is made up by conversion of a small fraction of the available center-of-mass collisional energy (2.86 keV) in an inelastic collision. It appears that the fraction of nondissociating **1** can be attributed to metastable electronic states produced by electron transfer. The deuterium substitution and precursor ion internal energy presumably affect the pertinent vibrational wave functions of the ground and excited electronic states of **1** and the dH/dQ coupling elements for nonradiative decay to the dissociative ground state.[34,35] The exact nature of these effects remains to be elucidated. Assuming that the higher excited electronic states are bound, one can also explain the unusual behavior of **1** in variable-time measurements, where less apparent dissociation was observed upon increasing the path length for radicals. This can be due to collisional excitation of the bound ^{2}A state of **1** to higher excited states. Since these are Rydberg-like states, they have greater cross sections for collisional ionization than those for the ^{2}A state and thus provide a higher yield of reionized $\mathbf{1}^+$. Similar effects caused by photoexcitation of low exited electronic states to higher Rydberg states have been reported previously.[36]

Conclusions

The aminodihydroxymethyl radical **1** is the first species in the family of electron-super-rich radicals that is formed in a long-lived metastable state. Computations indicate that the ground electronic state is bound but highly vibrationally excited when formed by collisional electron transfer. The main dissociation of **1** is loss of a hydroxyl hydrogen atom forming carbamic acid. Loss of an amine hydrogen atom is competitive only at high vibrational excitation energies and forms hydroxycarbimidic acid as a minor product. The metastable fraction of **1** is presumably due to long-lived (>4 μs) excited electronic states which are accessed by electron transfer because of favorable Franck−Condon factors.

Acknowledgment. Support of this work by the National Science Foundation (Grants CHE-0750048 for experiments and CHE-0342956 for computations) is gratefully acknowledged. The Computational Chemistry Center at the UW Department of Chemistry receives joint support from the NSF and the University of Washington. We thank Dr. Martin Sadilek for his technical assistance with mass spectra measurements. The JEOL HX-110 mass spectrometer was a generous donation from the former Seattle Biomembrane Institute by courtesy of Prof. S. Hakomori.

Supporting Information Available: Tables S1−S23 of optimized geometries in Cartesian coordinate format, total

B3LYP, MP2, and CCSD(T) energies, and zero-point energies. Figures S1 and S2 with CID and NR mass spectra. This material is available free of charge via the Internet at http://pubs.acs.org.

References and Notes

(1) Criegee, R.; Henecka, H.; Kurtz, P.; Petersen, S.; Piepenbrink, H.-F. In *Methoden der Organischen Chemie (Houben-Weyl)*; Muller, E., Ed.; Georg Thieme Verlag: Stuttgart, Germany, 1955; *Sauerstoff-Verbindungen, III,* p 141.

(2) Voet, D.; Voet, J. G.; Pratt, C. W. *Fundamentals of Biochemistry*; Wiley: New York, 1999; pp 173, 343, 622, 701.

(3) (a) Carpino, L. A.; Han, G. Y. *J. Org. Chem.* **1972**, *37*, 3404–3409. (b) Amblard, M. Fehrentz, J.-A.; Martinez, J.; Subra, G. In *Peptide Synthesis and Applications*; Howl, J., Ed.; Humama Press: Totowa, NJ, 2005, pp 3−24.

(4) For recent reviews, see: (a) Turecek, F. *Top. Curr. Chem.* **2003**, *225*, 77–129. (b) Schalley, C. A.; Hornung, G.; Schroder, D.; Schwarz, H. *Chem. Soc. Rev.* **1998**, *27*, 91–104.

(5) Van den Berg, K.; Lebrilla, C. B.; Terlouw, J. K.; Schwarz, H. *Chimia* **1987**, *41*, 122–124.

(6) (a) Curtis, P. M.; Williams, B. W.; Porter, R. F. *Chem. Phys. Lett.* **1979**, *65*, 296–299. (b) Burgers, P. C.; Holmes, J. L.; Mommers, A. A.; Terlouw, J. K. *Chem. Phys. Lett.* **1983**, *102*, 1–3. (c) Danis, P. O.; Wesdemiotis, C.; McLafferty, F. W. *J. Am. Chem. Soc.* **1983**, *105*, 7454–7456.

(7) (a) Schaftenaar, G.; Postma, R.; Ruttink, P. J. A.; Burgers, P. C.; McGibbon, G. A.; Terlouw, J. K. *Int. J. Mass Spectrom. Ion Proc.* **1990**, *100*, 521–544. (b) McGibbon, G. A.; Kingsmill, C. A.; Terlouw, J. K.; Burgers, P. C. *Org. Mass Spectrom.* **1992**, *27*, 126–134. (c) Burgers, P. C.; McGibbon, G. A.; Terlouw, J. K. *Eur. Mass Spectrom.* **1995**, *1*, 261–268.

(8) Gerbaux, P.; Tureček, F. *J. Phys. Chem. A* **2002**, *106*, 5938–5950.

(9) Hao, C.; Seymour, J. L.; Tureček, F. *J. Phys. Chem. A* **2007**, *111*, 8829–8843.

(10) McMahon, A. W.; Chowdhury, S. K.; Harrison, A. G. *Org. Mass Spectrom.* **1989**, *24*, 620–624.

(11) (a) Burkey, T. J.; Castelhano, A. L.; Griller, D.; Lossing, F. P. *J. Am. Chem. Soc.* **1983**, *105*, 4701–4703. (b) Shaffer, S. A.; Turecek, F.; Cerny, R. L. *J. Am. Chem. Soc.* **1993**, *115*, 12117–12124.

(12) Modarresi-Alam, A. R.; Rostamizahed, M.; Najafi, P. *Turk. J. Chem.* **2006**, *30*, 269–276.

(13) Tureček, F.; Gu, M.; Shafer, S. A. *J. Am. Soc. Mass Spectrom.* **1992**, *3*, 492–501.

(14) (a) Kuhns, D. W.; Tran, T. B.; Shaffer, S. A.; Tureček, F. *J. Phys. Chem.* **1994**, *98*, 4845–4853. (b) Kuhns, D. W.; Tureček, F. *Org. Mass Spectrom.* **1994**, *29*, 463–469.

(15) Frisch, M. J.; Trucks, G. W.; Schlegel, H. B.; Scuseria, G. E.; Robb, M. A.; Cheeseman, J. R.; Montgomery, J. A., Jr.; Vreven, T.; Kudin, K. N.; Burant, J. C.; Millam, J. M.; Iyengar, S. S.; Tomasi, J.; Barone, V.; Mennucci, B.; Cossi, M.; Scalmani, G.; Rega, N.; Petersson, G. A.; Nakatsuji, H.; Hada, M.; Ehara, M.; Toyota, K.; Fukuda, R.; Hasegawa, J.; Ishida, M.; Nakajima, T.; Honda, Y.; Kitao, O.; Nakai, H.; Klene, M.; Li, X.; Knox, J. E.; Hratchian, H. P.; Cross, J. B.; Bakken, V.; Adamo, C.; Jaramillo, J.; Gomperts, R.; Stratmann, R. E.; Yazyev, O.; Austin, A. J.; Cammi, R.; Pomelli, C.; Ochterski, J. W.; Ayala, P. Y.; Morokuma, K.; Voth, G. A.; Salvador, P.; Dannenberg, J. J.; Zakrzewski, V. G.; Dapprich, S.; Daniels, A. D.; Strain, M. C.; Farkas, O.; Malick, D. K.; Rabuck, A. D.; Raghavachari, K.; Foresman, J. B.; Ortiz, J. V.; Cui, Q.; Baboul, A. G.; Clifford, S.; Cioslowski, J.; Stefanov, B. B.; Liu, G.; Liashenko, A.; Piskorz, P.; Komaromi, I.; Martin, R. L.; Fox, D. J.; Keith, T.; Al-Laham, M. A.; Peng, C. Y.; Nanayakkara, A.; Challacombe, M.; Gill, P. M. W.; Johnson, B.; Chen, W.; Wong, M. W.; Gonzalez, C.; Pople, J. A. *Gaussian 03*, revision B.05; Gaussian, Inc.: Pittsburgh, PA, 2003.

(16) (a) Becke, A. D. *J. Chem. Phys.* **1993**, *98*, 1372–1377. (b) Becke, A. D. *J. Chem. Phys.* **1993**, *98*, 5648–5652. (c) Stephens, P. J.; Devlin, F. J.; Chablowski, C. F.; Frisch, M. J. *J. Phys. Chem.* **1994**, *98*, 11623–11627.

(17) Rauhut, G.; Pulay, P. *J. Phys. Chem.* **1995**, *99*, 3093–3100.

(18) Dunning, T. H., Jr. *J. Chem. Phys.* **1989**, *90*, 1007–1023.

(19) Cízek, J.; Paldus, J.; Sŕoubková, L. *Int. J. Quantum Chem.* **1969**, *3*, 149–167.

(20) Purvis, G. D.; Bartlett, R. J. *J. Chem. Phys.* **1982**, *76*, 1910–1918.

(21) Stratmann, R. E.; Scuseria, G. E.; Frisch, M. J. *J. Chem. Phys.* **1998**, *109*, 8218–8224.

(22) Foresman, J. B.; Head-Gordon, M.; Pople, J. A.; Frisch, M. J. *J. Phys. Chem.* **1992**, *96*, 135–149.

(23) Gilbert, R. G.; Smith, S. C. *Theory of Unimolecular and Recombination Reactions*; Blackwell Scientific Publications: Oxford, U.K., 1990; pp 52−132.

(24) Zhu, L.; Hase, W. L. *Quantum Chemistry Program Exchange*, Program No. QCPE 644; Indiana University: Bloomington, IN, 1994.

(25) Frank, A. J.; Sadílek, M.; Ferrier, J. G.; Tureček, F. *J. Am. Chem. Soc.* **1997**, *119*, 12343–12353.

(26) NIST Standard Reference Database Number 69. http://webbook.nist.gov/chemistry (September 2008).

(27) Kaur, D.; Kaur, R. P.; Kaur, P. *Bull. Chem. Soc. Jpn.* **2006**, *79*, 1869–1875.

(28) Remko, M. *Collect. Czech. Chem. Commun.* **1988**, *53*, 1141–1148.

(29) Fitch, W. L.; Sauter, A. D. *Anal. Chem.* **1983**, *55*, 832–835.

(30) Nguyen, V. Q.; Shaffer, S. A.; Tureček, F.; Hop, C. E. C. A. *J. Phys. Chem.* **1995**, *99*, 15454–15464.

(31) Aoyagi, M.; Kato, S. *J. Chem. Phys.* **1988**, *88*, 6409–6418.

(32) Tureček, F. *Int. J. Mass Spectrom.* **2003**, *227*, 327–338.

(33) Wolken, J. K.; Tureček, F. *J. Phys. Chem. A* **1999**, *103*, 6268–6281.

(34) Fischer, G. *Vibronic Coupling*; Academic Press: London, 1984; pp 2952.

(35) Tureček, F.; Reid, P. J. *Int. J. Mass Spectrom.* **2003**, *222*, 49–61.

(36) Nguyen, V. Q.; Sadílek, M.; Frank, A. J.; Ferrier, J. G.; Tureček, F. *J. Phys. Chem. A* **1997**, *101*, 3789–3799.

JP9019987